Wave overtopping on a low-crested seawall under extreme waves

Qingfei Gao (高庆飞) [a], Tong Wang (王统) [a], Matteo Rubinato [b], Zhuqin Liu (刘竹琴) [c], Xizeng Zhao (赵西增) [c], Min Luo (罗敏) [c*]

[a] School of Transportation Science and Engineering, Harbin Institute of Technology, Harbin 150090, China

[b] Department of Civil Engineering, College of Engineering and Physical Sciences, Aston University, Birmingham, B4 7ET, UK

[c] Ocean College, Zhejiang University, Zhoushan 316021, Zhejiang, China

Abstract

Extreme waves in global nearshore regions, frequently accompanied by wave setup, can transform seawalls into low-crested structures. Such events pose threats to coastal infrastructure due to enhanced overtopping and intense hydrodynamic loads imposed on seawalls and related coastal defenses. This study investigates the wave overtopping dynamics on a low-crested seawall under extreme wave conditions through controlled wave flume experiments that have comprehensively measured wave elevations, free-surface profiles, overtopping volumes and impact pressures. The temporal and spatial characteristics of wave overtopping and their dependence on water depth and wave parameters are examined. The results demonstrate a positive correlation between overtopping volume and wave amplitude, with localized impact pressures also intensifying as wave amplitude increases. Conversely, as wave peak frequency increases and seawall crest elevation rises, waves, especially those of larger amplitudes, tend to break earlier on the seaward slope. This earlier breaking dissipates a significant portion of wave energy, thereby reducing overtopping volumes and the impact pressures on the seawall. Furthermore, the study reveals that as the focusing position of the extreme wave group shifts landward, there is a notable reduction in the group's cumulative energy. This energy attenuation results in diminished overtopping volumes and lower impact loads. These findings elucidate the complex interplay between wave parameters, seawall height and the dynamics of wave overtopping under extreme wave conditions, as well as provide a theoretical framework for optimizing the design and resilience of seawalls to mitigate the adverse impacts of extreme wave events on coastal infrastructure.

Keywords: Wave overtopping; Seawall; Wave flume experiment; Extreme wave; Wave impingement

* Corresponding author, E-mail: min.luo@zju.edu.cn (M. Luo).

1. Introduction

With global climate change, the frequency and intensity of extreme waves along the coast of the world are increasing (Dysthe et al., 2008, Li et al., 2024, Lobeto et al., 2024). These extreme waves are often accompanied by rapid coastal water level rises, transforming existing seawalls into low-crested structures, with a relative crest elevation of $0 \leq R_c/H_0 < 1.5$ (Van der Meer et al., 2018). Such conditions lead to excessive overtopping volumes as seawater surges over seawalls, resulting in coastal flooding, economic losses, and structural damage (Nikolkina and Didenkulova, 2012). Wave breaking during interactions between extreme waves and seawalls generates intense slamming pressures that further impact seawalls and nearby infrastructure (Qu et al., 2022, Wang et al., 2025). Consequently, investigating the hydrodynamic mechanisms of overtopping on low-crested seawalls under extreme wave conditions is essential for designing resilient seawall structures, protecting coastal cities and enhancing disaster mitigation efforts.

Wave overtopping can cause severe flooding and waterlogging behind seawalls. Substantial research efforts have been devoted to the characteristics and prediction of overtopping volume (Paape, 1960, Owen and Steele, 1993, Van der Meer et al., 2018). Over the past two decades, advancements in experimental methods have enhanced the understanding of seawall overtopping dynamics. Hughes and Thornton (2016) analyzed overtopping volumes' temporal variation and identified a peak overtopping volume several times greater than the average followed by a gradual decline. Some studies, e.g., Van der Meer et al. (2010), Chen et al. (2015), Mares-Nasarre et al. (2019) and van Bergeijk et al. (2019), investigated overtopping flow depths and velocities on seawalls' horizontal crests and found that the overtopping flow depths decrease exponentially with distance from the crest edge although different decay rates were used across studies. Gallach-Sánchez et al. (2021) conducted experimental investigations into the overtopping of steep, low-crested seawall structures induced by non-breaking irregular waves, with an emphasis on how wave characteristics influence the distribution of overtopped water and associated impact dynamics. Esteban et al. (2022) explored overtopping discharge around a fixed vertical cylinder under non-impulsive wave conditions using a combination of experimental and numerical methodologies. More recently, Wong and Chow (2024) performed numerical simulations using OpenFOAM to analyze the wave run-up and overtopping characteristics of ocean swells propagating over varying seabed bathymetries. Rif'atin et al. (2024) investigated the effectiveness of stepped revetments in reducing wave run-up height and overtopping discharge by invoking the Genetic Algorithm for optimization.

Recent studies have increasingly focused on the wave overtopping induced by a solitary wave, which is a typical example of extreme wave events. For example, Hsiao and Lin (2010) investigated the solitary wave overtopping and impinging process through experiments and numerical simulations and highlighted the high risks of extreme wave impacts in the condition of rising water levels. Baldock et al. (2012) experimentally studied the overtopping by solitary waves and found that overtopping rates increased linearly with the deficit in the wave run-up freeboard. Luo et al. (2019) have applied the Consistent Particle Method (CPM) to simulate the solitary wave overtopping process and the results have suggested that higher water levels can result in much more overtopping volume. Despite these progresses, most relevant studies have focused on overtopping volumes, e.g., Goda (2009), Nørgaard et al. (2014), Van Doorslaer et al. (2015), Pan et al. (2015), Hughes and Thornton (2016), Molines et al. (2019), Van der Meer et al. (2018), Salauddin and Pearson (2019), etc. Some studies have been devoted to examining the hydrodynamic processes of wave overtopping, e.g. nonlinear wave breaking, energy dissipation along the seawall, and violent wave impacts on the seawall. However, relevant studies have primarily considered regular (Wen et al., 2019, Adibhusana et al., 2023), irregular (Liu et al., 2020, Koosheh et al., 2024), solitary waves (Hsiao et al., 2008, Huang et al., 2022) or tidal bores (Qu et al., 2024) and few have touched extreme waves. Considering the destructive effects of extreme waves on coastal infrastructures, it is crucially important to reveal the dynamic process and overtopping mechanisms of extreme waves on low-crested seawalls for better protection of coastal areas.

Overtopping flows can apply violent impact loads on seawalls and cause damage to coastal infrastructures. In studies of wave overtopping loads, Oumeraci et al. (1993) classified wave-breaking types and qualitatively linked slamming forces to wave shapes. Neelamani et al. (1999) established empirical formulas for wave pressure prediction, emphasizing reflection and phase shifts. Cuomo et al. (2010) conducted experiments within the VOWS (Violent Overtopping by Waves at Seawalls) framework and observed discrepancies between empirical predictions and experimental data of wave impact loads. In the combined experimental and numerical work by Hsiao and Lin (2010), the authors found that the maximum dynamic net wave force on the seawall caused by solitary wave overtopping typically corresponded to the peak surface elevations during overtopping. In the CPM simulation study of Luo et al. (2019), it has been demonstrated that front slope angles significantly influence the forces induced by overtopping flows. Qu et al. (2022) have shown that wind enhances wave propagation and intensifies wave impact loads on a seawall. Recent research has examined the threats posed by wave overtopping to pedestrians on coastal seawalls (Cao et al., 2021, Chen et al., 2021, Zhao et al., 2024), focusing on the characteristics of overtopping flow depths and impact forces, as well as predictive methodologies. Liu et al. (2023) investigated the dynamic response of viscoelastic floating covers under wave overtopping conditions through Smoothed Particle Hydrodynamics simulations. While significant progress has been made in understanding the dynamic processes of wave overtopping on seawalls, critical questions remain regarding the behavior of overtopping characteristics and loads under extreme wave conditions and their dependence on wave parameters.

This study investigates wave overtopping on a low-crested seawall under extreme wave conditions through controlled wave flume experiments. A 1/16 scale model of a seawall section was constructed. An increased water depth relative to the scaled on-site water depth was considered to simulate low-crest scenarios, representing water level rises due to short-term wave setups. Extreme waves were generated using the focused wave theory with specified amplitudes and frequency bands. Comprehensive measurements were conducted, including wave elevations, deformed wave profiles, impact pressures and overtopping volumes. Detailed analyses were performed on the morphological features, energy evolutions, overtopping volumes and impact pressures of the wave overtopping flows, as well as their correlations with the water depth and wave parameters. The experimental methodology is presented in Section 2, results and discussion in Section 3, and conclusions in Section 4.

2. Experimental methodology

2.1. Experimental model setup

The physical model experiments were conducted in a wave flume at Zhejiang University. The wave flume, 35 m in length, 0.6 m in width, and 0.8 m in depth, is equipped with a piston-type wave generator capable of generating both regular and irregular waves, as shown in Fig. 1(a). Unidirectional waves were considered in experiments and a scaled seawall with a uniform cross section (along the flume width direction) was deployed in the wave flume. The cross-section of the experimental seawall was modeled after typical coastal seawalls found along Zhejiang coastlines and a model scale ratio of λ_l = 1/16 was adopted. The physical model comprised three main components:

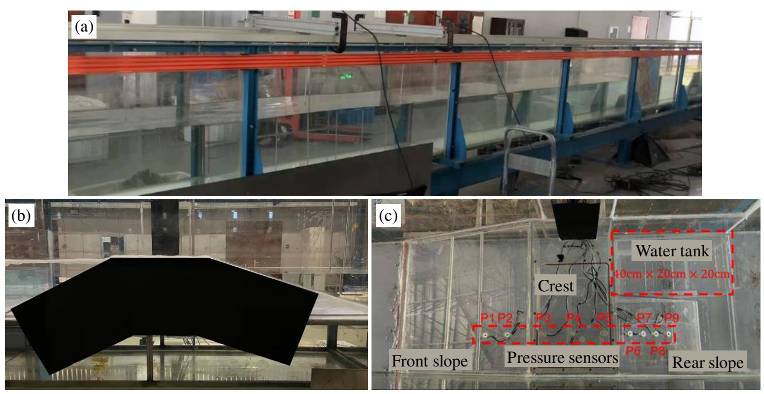

Fig. 1. Experimental setup: (a) Wave flume; (b) Seawall model; (c) Overtopping collection tank.

(1) Slope bottom: representing the natural seabed, a gradient of 1:20 was employed. This slope was located 10 m from the wave generator and extended 5 m in length.

(2) Seawall structure: an impermeable seawall was constructed with a front slope of 1:3, a crest height of 0.45 m, a crest width of 0.325 m, and a rear slope of 1:2 extending 0.4 m, as shown in Fig. 1(b).

(3) Overtopping collection system: positioned on the rear slope, a tank with dimensions of 0.4 m × 0.2 m × 0.2 m was used to collect overtopping water, as shown in Fig. 1(c).

To ensure a watertight assembly, silicone sealant was applied to fill gaps between the sloped bottom, seawall, flat bottom, and flume sidewalls. The experimental setup is illustrated in Fig. 2.

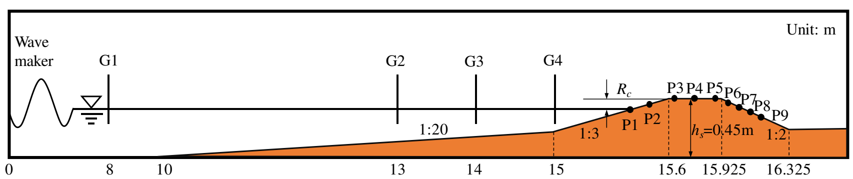

Fig. 2. Schematic view and key dimensions of the experimental setup of wave overtopping on a low-crested seawall. The *x* coordinates of the pressure measurement points, i.e., P1 – P9, are x_{P1} = 15.4 m, x_{P2} = 15.5 m, x_{P3} = 15.64 m, x_{P4} = 15.7625 m, x_{P5} = 15.885 m, x_{P6} = 15.985 m, x_{P7} = 16.045 m, x_{P8} = 16.105 m, and x_{P9} = 16.165 m. The *x* coordinates of the wave elevation measurement points, i.e., G1 – G4, are x_{G1} = 8 m, x_{G2} = 13 m, x_{G3} = 14 m, and x_{G4} = 15 m.

2.2. Measurement devices

The following instrumentation was deployed during the experiments:

(1) Wave gauges: Four KENEN capacitive wave gauges were installed at 8 m (G1), 13 m (G2), 14 m (G3), and 15 m (G4) from the wave generator to record free surface elevations. The wave gauges have a full scale of -0.25 m to 0.25 m, a measurement resolution of 10^{-4} m, and a sampling frequency of 100 Hz.

(2) Pressure sensors: nine piezoresistive pressure sensors were deployed to measure wave impact pressures on the seawall induced by overtopping flows. Two sensors were placed on the front slope, three on the crest, and four on the rear slope, with their precise locations detailed in Fig. 2. The pressure sensors have a measurement full scale of 5 kPa, a measurement resolution of 0.5% full scale, and a sampling frequency of 400 Hz.

(3) Overtopping volume measurement: the collected overtopping water was weighed and converted to volume, which was then divided by the tank's width (B = 0.2 m) to get the overtopping volume per unit width.

(4) High-speed camera: An FR400 high-speed camera was adopted to capture the evolution of the water surface morphology during wave overtopping, providing detailed visual data of wave-seawall interactions. The camera has a sampling frequency of 100 Hz and a resolution of 2048 × 2048 pixels.

2.3. Wave generation methodology

In this study, extreme waves were modeled using the focused wave theory, which simulates the dispersive focusing of a series of wave components. The wave elevation η is expressed as:

$$\eta(x,t)=\sum_{i=1}^{N}a_i\cos\left(k_i\left(x-x_{\mathrm{f}}\right)-2\pi f_i\left(t-t_{\mathrm{f}}\right)\right) \tag{1}$$

where, N is the number of wave components and N = 30 is adopted in the present study; a_i, k_i and f_i are the amplitude, wave number, and frequency of the i-th wave component, respectively. The terms x_{f} and t_{f} denote the focusing location and time of the wave group, respectively. The amplitude a_i of each wave component is determined by considering the JONSWAP (Joint North Sea Wave Project) wave spectrum (Goda, 2010), which reads:

$$S(f)=\beta_{\mathrm{J}}H_{\mathrm{s}}^2 f_{\mathrm{p}}^4 f^{-5}\exp(-1.25(f/f_{\mathrm{p}})^{-4})\gamma^{\exp\left(-\frac{(f/f_{\mathrm{p}}-1)^2}{2\sigma^2}\right)} \tag{2}$$

with

$$\beta_J=\frac{0.06238}{0.230+0.0336\gamma-0.185(1.9+\gamma)^{-1}}(1.094-0.01915\ln(\gamma)) \tag{3}$$

and

$$\sigma=\begin{cases}0.07 & \text{if } f\le f_p\\ 0.09 & \text{if } f>f_p\end{cases} \tag{4}$$

where f_{p} is the peak frequency; Hs is the significant wave height and is two times the amplitude of the focused wave at the focusing location (i.e., A_{P}); γ is the peak enhancement factor and is taken to be 3.3. With the wave spectrum density value for a wave component of frequency f_i, i.e., $S(f_i)$ and the amplitude of the focused wave at the focusing location (i.e., A_{P}), the amplitude of the i-th wave component can be calculated as:

$$a_i=A_{\mathrm{p}}\frac{S\left(f_i\right)\Delta f}{\sum_{i=1}^{N}S\left(f_i\right)\Delta f} \tag{5}$$

where the angular frequency range Δf is defined as $\Delta f=\frac{f_{\max}-f_{\min}}{N}$, with $f_{\max}$ and $f_{\min}$ being the upper and lower limits of the wave frequency band.

2.4. Experimental cases

The experimental parameters were designed to reflect realistic coastal conditions in Zhejiang Province, China. By considering the experimental scale ratio, the first experimental water depth was set at h = 0.40 m, representative of the typical coastal depths. The second depth was h = 0.45 m, which took into account the water level rises due to storm surges and long-term sea-level rise. Correspondingly, the crest elevations were R_c = 0.05 m and 0 m. The wave amplitudes (i.e., A_p) of 0.06 m, 0.07 m and 0.08 m were selected, along with frequencies (i.e., f_p) of 0.6 Hz、0.8 Hz and 1.0 Hz. Considering the randomness in the focusing location of extreme waves near the coast, seven focusing locations (i.e., x_f) ranging from 12 m to 15 m with an interval of 0.5 m were investigated. With these, a total of 126 test cases were established, as summarized in Table 1.

Table 1. Summary of experimental cases

Parameters	Values		
h (m)	0.4, 0.45		
R_c (m)	0.05, 0		
x_f (m)	12, 12.5, 13, 13.5, 14, 14.5, 15		
A_p (m)	0.06, 0.07, 0.08		
f_p (Hz)	0.6	0.8	1.0
[f_{min}, f_{max}]	[0.3, 0.9]	[0.5, 1.1]	[0.7, 1.3]

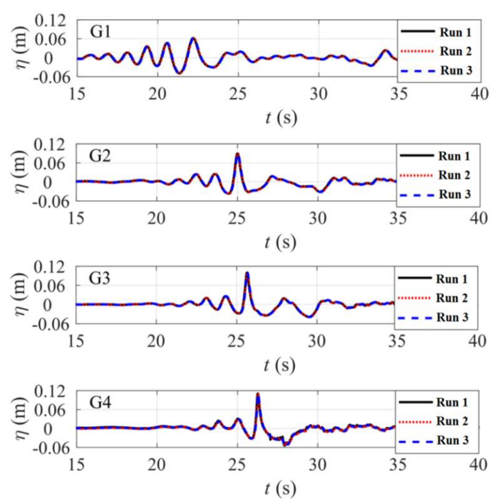

Fig. 3. Wave height time series of three independent repeated tests for the case of R_c = 0 m, A_p = 0.08 m, f_p = 0.6 Hz and x_f = 13 m.

2.5. Repeatability of experimental data

Experimental cases were repeated three times to ensure consistency. As an example, the wave elevations and impact pressures for three repeated runs of the case characterized by R_c = 0 m, A_p = 0.06 m, f_p = 0.6 Hz and x_f = 13 m are shown in Figs. 3 and 4, respectively. The results demonstrate that the wave heights and pressure time histories across the three independent repetitions nearly overlap, with a relative error of less than 2%. The average overtopping volume measured across the three tests was 41.1 L/m, with an average relative error of just 0.49%. These findings highlight the good repeatability of the wave generation system and the reliability of the measurement devices, confirming the accuracy of the experimental data.

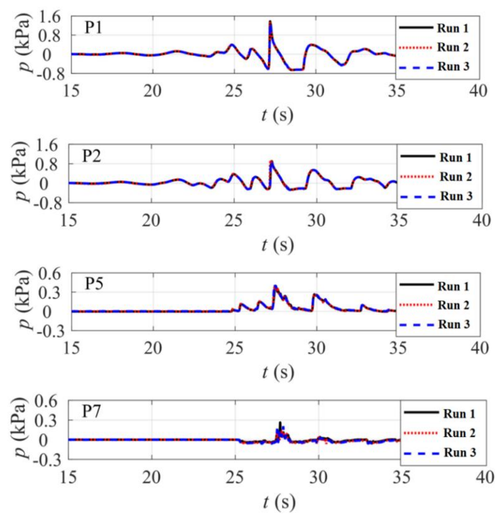

Fig. 4. Pressure time series of three independent repeated tests for the case of R_c = 0 m, A_p = 0.08 m, f_p = 0.6 Hz and x_f = 13 m.

3. Results and discussion

3.1. Hydrodynamic characteristics of overtopping flows

To examine the hydrodynamic variations during the overtopping process of extreme waves on low-crested seawalls, this section considers specific standard test conditions, including a spectral peak frequency f_p = 0.6 Hz, wave amplitude A_p = 0.08 m, focusing location x_f = 13 m, and seawall crest elevations R_c = 0 m and 0.05 m. These parameters were selected to facilitate a mechanistic analysis of hydrodynamic characteristics during overtopping under extreme wave conditions. The investigation focuses on the overtopping patterns of extreme waves and the evolution of free surface elevations and the corresponding wave energy.

3.1.1. Overtopping morphology evolution

The wave run-up and overtopping morphology for $R_c = 0$ m at representative time steps are shown in Fig. 5. As the wave runs up along the sloping beach, the phenomenon of local water level dropping, i.e., wave setdown, happens. Then, the leading edge of the primary wave crest steepens and plunges to form wave breaking (Fig. 5a) and entraps some air (Fig. 5b). Subsequently, the plunging breaker impacts on the front slope of the seawall, generating white splashes (Fig. 5c). As the wave continues its run-up, the air pocket disintegrates entirely, generating sprays and a violent jet striking the seawall crest (Fig. 5d), and the bubbly flows result in significant energy dissipations. The overtopping water further generates an upward-impinging breaking wave near the crest's front edge, with the bubbly flow transitioning into a rapid-moving jet across the rear crest edge (Fig. 5e). After that, a secondary wave crest (hereafter termed the "secondary trailing crest") reaches the seawall's front slope without breaking and causes more overtop flows Fig. 5f). Also note that Fig. 5(a), (c), (e), and (g) respectively correspond to the wave profiles when the pressure peaks at P1, P2, P3, and P5 occur. As can be seen that the pressure peaks are primarily caused by breaking wave impacts.

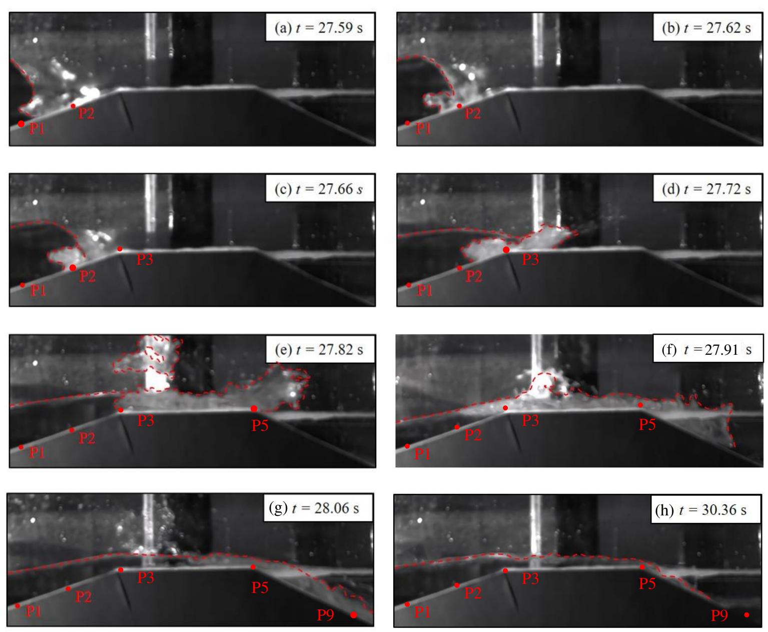

Fig. 5. Profiles of wave run-up and overtopping at typical time instants for the seawall crest elevation of $R_c = 0$ m.

For the case of $R_c = 0.05$, the morphologies of the overtopping flow show notable differences as presented in Fig. 6. Specifically, the primary wave crest does not form a well-shaped air pocket along the front slope. Instead, the front edge becomes unstable, detaching in large segments and deforming violently (Fig. 6b). The violent breaking of the primary crest produces a jet flow at the crest's front edge (Fig. 6c) and forms well-developed bubbly flows at the seawall crest (Fig. 6d). Interestingly, subsequent waves following the bubbly flows interact with incoming waves at the crest, producing a seaward-directed jet at the crest's front edge (Fig. 6e). This seaward jet behavior contrasts with the upward-impinging breaking wave observed in the case of $R_c = 0$ (Fig. 5e). For the secondary trailing crest, no significant differences in overtopping morphology are observed between the two cases, with neither condition inducing breaking of the trailing crest. In summary, the seawall crest elevation (R_c) primarily influences the overtopping behavior of the primary wave crest, intensifying breaking processes and enhancing bubbly flow development while reducing overtopping intensity. Conversely, the crest elevation has negligible effects on the overtopping morphology of the secondary trailing crest.

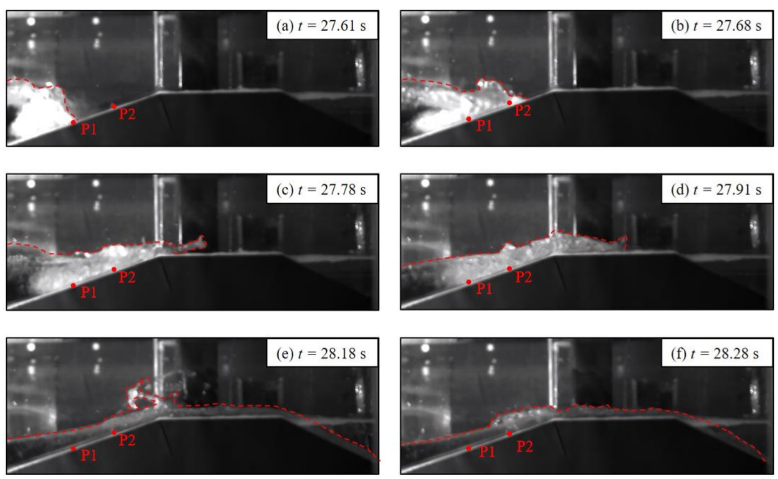

Fig. 6. Profiles of wave run-up and overtopping at typical time instants for the seawall crest elevation of $R_c = 0.05$ m.

3.1.2. Spatio-temporal evolution of wave elevations and energy

In the process of wave run-up along the sloping seawall, wave shoaling and breaking occur. These are accompanied with wave energy transports and evolutions, which directly affect the wave impact loads applied on the seawall and the overtopping volume. Therefore, the spatiotemporal evolutions of the wave elevations and their energy at typical locations are studied based on the representative case of R_c = 0 m, f_p = 0.6 Hz, A_p = 0.08 m and x_f = 13 m (this case is characterized by violent wave run-up and overtopping). The time-frequency energy characteristics of the wave train are analysed by the Morlet wavelet transform (Grossmann and Morlet, 1984, Jiang et al., 2018).

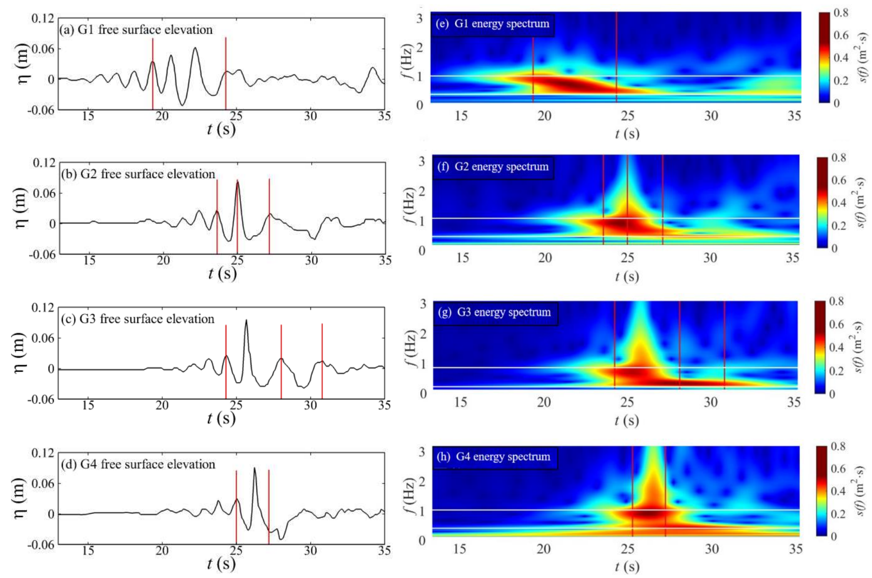

Fig. 7. Time series of free surface elevations at G1-G4 (the left column) and the spatiotemporal energy evolutions (the right column).

At a location on the flat bed and 2 m away from the sloping beach toe (i.e., G1), relatively smaller free surface elevations of the wave group are observed (Fig. 7a). The time-spectral contour of wave energy (Fig. 7e) shows that the wave energy focuses to some extent between t =19.56 s to 23.69 s. The peak wave energy of the wave train reaches 14.6 $m^2 \cdot s$ upon the arrival of the primary wave crest at t = 20.3 s. At the wave focusing location (i.e., G2), the wave group attains a large wave height (Fig. 7b) with an almost symmetrical pattern for the primary crest. The energy spectrum contour (Fig. 7f) shows that during t = 23.55 s to 25 s, shallower water depths amplify nonlinear effects, shifting energy from the primary frequency to higher frequencies. The total wave group energy reaches 19.5 $m^2 \cdot s$. After the secondary wave crest, low-frequency wave components of certain energy pass through G2, and the energy is slightly higher than that at G1 after the secondary wave crest passes.

At G3 that is 1 m towards the coast, the primary wave crest becomes steeper and higher and less symmetric compared to that at G2 (Fig. 7c). Energy shifts from the primary frequency to higher frequencies during t = 24.29 s to 25.7 s. The time instants coincide with the arrival time of the secondary and primary wave crests (Fig. 7g). The shoaling effect at this location increases the amplitude and energy of the primary crest, peaking at 20.7 $m^2 \cdot s$. After the secondary crest passes, waves with frequencies above 0.54 Hz propagate beyond G3, with energy concentrated between 0.3 Hz and 0.54 Hz.

At the seawall toe (i.e., G4), the shoaling effect intensifies further, which cause further increase of the primary wave crest and pronounced asymmetry between the adjacent secondary crests at both sides (Fig. 7d). Upon the primary crest's arrival (t = 26.28 s), the wave group energy reaches its maximum of 26.2 $m^2 \cdot s$ (Fig. 7h). It can be seen from the energy spectrum contour that the wave energy shifts to both the high- and low-frequency ranges during the running up process. This is related to the fact that the reduced water depth causes the phase delay of the low-frequency long waves. Besides, high-frequency wave components break on the seawall, releasing some wave energy, and some wave energy is reflected back to the sea. These lead to an increase in the low-frequency wave energy at G4.

3.2. Variation of wave energy evolutions with wave parameters and water depth

The wave energy evolution features during the wave run-up and overtopping process vary with the wave parameters (e.g., wave focusing location x_f and the spectral peak frequency f_p) and the water depth (which is related to the crest elevation R_c). These variations are critical to understanding the mechanisms of the overtopping behaviors induced by extreme waves. This section explores these influences based on the standard case (with the parameters of R_c = 0 m, A_p = 0.08 m, f_p = 0.6 Hz and x_f = 13 m) by analyzing the wave energy characteristics at locations G1 to G4.

3.2.1. Influences of wave focusing location

Fig. 8 (a) illustrates how the shift in wave focusing location (i.e., x_f) alters the wave group energy. As the focusing location moves towards the shoreline, the low-frequency wave energy decreases significantly and its duration shortens; the high-frequency energy also slightly decreases; the wave energy concentrates more around the primary frequency. Specifically, when x_f shifts from 12 m to 15 m, the maximum energy of the wave group at G4 decreases from 26.2 m^2 to 24.7 m^2. These phenomena are primarily attributed to two reasons. Firstly, with the increase in x_f, the energy focus of the wave train is less developed at G4, and hence the wave height at G4 decreases (see Fig. 8 b). Secondly, the water depth at the wave focusing location becomes shallower as x_f moves towards the shoreline and the nonlinearity of the wave group is intensified. Hence, more wave components reach their maximum steepness and break, leading to more energy dissipations. These two reasons result in the reduction of the overtopping volume.

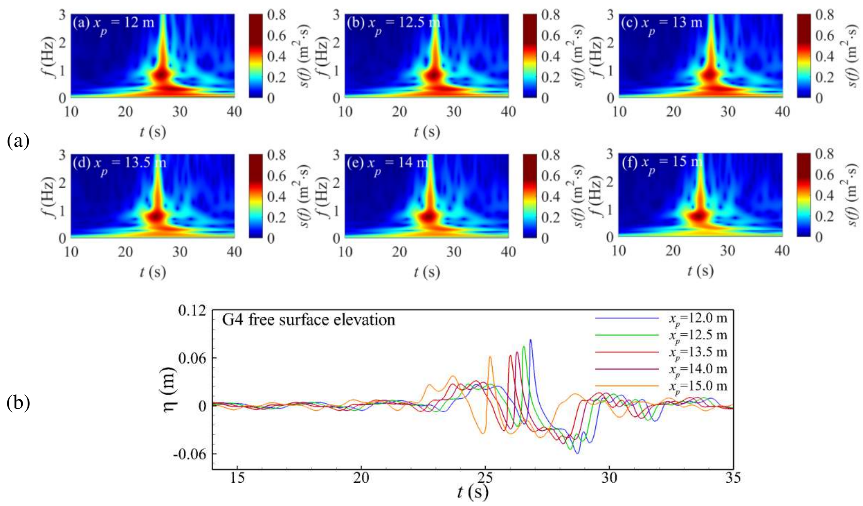

Fig. 8. Energy spectra and time histories of wave elevations at G4 in cases of different x_f.

3.2.2. *Influences of spectral peak frequency*

The spectral peak frequency (f_p) determines the energy distribution within the wave group and influences the energy evolution along the wave propagation and run-up process. This section compares the energy spectra of wave elevations at locations G1-G4 for three different spectral peak frequencies, i.e., f_p = 0.6 Hz, 0.8 Hz and 1.0 Hz. As shown in Fig. 9, the frequency ranges of waves with non-negligible energy for the three f_p values match the frequency ranges of the energy input from the wave generator. As f_p increases, in general, the energy distributions of the waves at G1-G4 all shift towards higher frequencies. More specifically, when f_p = 0.6 Hz the wave group contains more low-frequency wave energy particularly at location G4, whereas at f_p = 0.8 Hz and 1.0 Hz, the wave energy mainly concentrates around the peak frequency, with only a small portion of the wave energy transferring to the high- and low-frequency ranges. Besides, as the spectral peak frequency increases, the frequency ranges of energy distributions narrow especially at G2-G4, implying the wave energy becomes more concentrated. Moreover, the increase of f_p intensifies wave breaking, and hence more wave energy is dissipated during the wave run-up process.

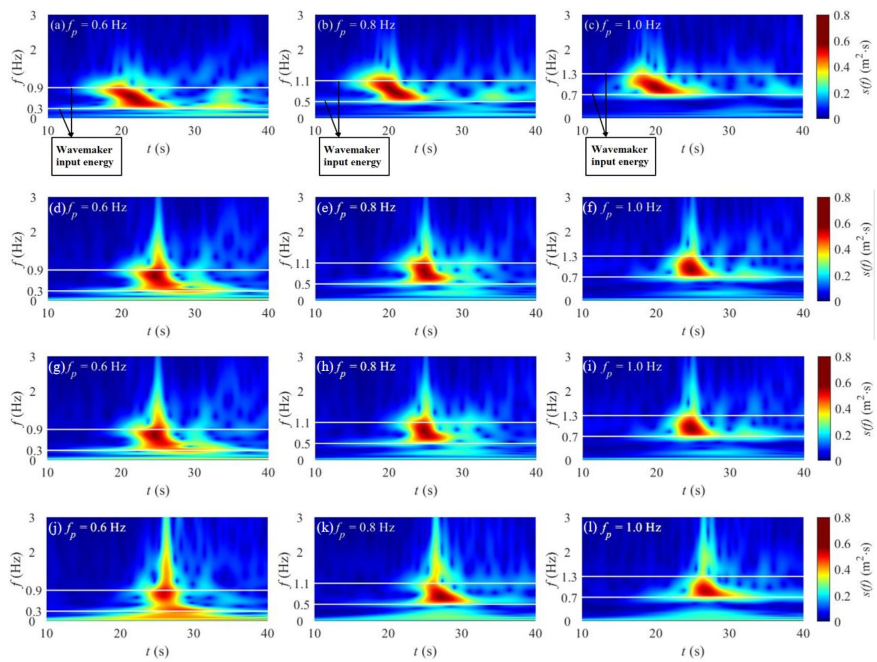

Fig. 9. Energy spectra of the wave elevation series at G1-G4 (the first to fourth rows, respectively) for different spectral peak frequencies f_p (R_c = 0 m, A_p = 0.08 m, x_f = 13.0).

3.2.3. *Influences of seawall crest elevation*

The water depth or crest elevation (R_c) significantly affects the wave energy evolution during the wave run-up and overtopping. To investigate this, the wave elevations at G1-G4 for the cases of R_c = 0 m and 0.05 m, A_p = 0.08 m, f_p = 0.6 Hz and x_f = 13 m are studied. As can be seen from Fig. 10, minor differences exist in the wave energy spectra at G1 for R_c = 0 m and 0.05 m, because G1 is relatively far from the wave focusing point and the nonlinear interactions among wave components are not intensive. At the wave focusing location G2, in the case of R_c = 0.05 m, more wave energy in the primary frequency range shifts to the low and high-frequency ranges. This is attributed to the shallower water depth, in which the nonlinear interactions among wave components and wave breaking are more significant, increasing the wave energy in low frequencies. At G3, the high-frequency wave energy for R_c = 0.05 m is significantly reduced compared to R_c = 0 m, while after the primary wave crest passes the wave energy spectra for both seawall crests show little differences. At G4, wave breaking happens in both cases; hence the low-frequency components are significant in the wave energy spectra.

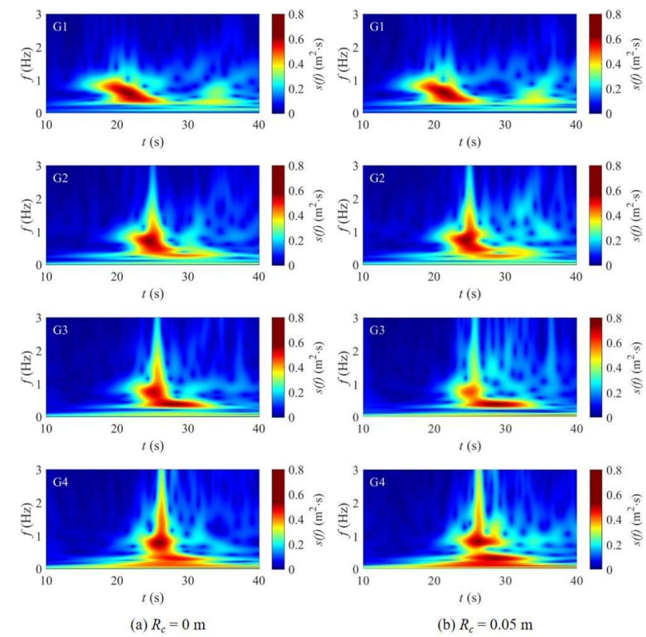

Fig. 10. Energy spectra of the wave elevation series at G1-G4 for different seawall crest elevations: (a) R_c = 0 m; (b) R_c = 0.05 m (A_p = 0.08 m, f_p = 0.6 Hz, x_f = 13.0).

3.3. Variation of overtopping volumes with wave parameters and water depth

This section examines the overtopping volume per unit width of extreme waves on a low-crested seawall (referred as "overtopping volume" hereafter) and analyzes its variations with the factors, such as the wave group amplitude A_p, wave focusing location x_f, spectral peak frequency f_p, and seawall crest elevation R_c.

3.3.1. Influences of wave amplitude

This section investigates the variation of wave overtopping volume with the focusing wave amplitude A_p and wave focusing locations x_f under the condition of R_c = 0 m. As illustrated in

Fig. 11, for fixed R_c, f_p and x_f, the overtopping volume exhibits an almost linear increase with the focusing amplitude. For the three studied spectral peak frequencies, the rates of increase in overtopping volume when A_p rises from 0.06 m to 0.08 m are 41.1%, 37.0% and 52.2%, respectively, with the average value being 43.5%. The maximum overtopping volume observed in the studied cases is 40.50 L/m, occurring in the case of R_c = 0 m, f_p = 0.6 Hz, A_p = 0.08 m and x_p = 12.0 m. Conversely, the minimum overtopping volume, 12.12 L/m, is observed in the case of $R_c = 0$ m, $f_p = 0.6$ Hz, $A_p = 0.06$ m and $x_p = 15.0$ m. In summary, these findings emphasize that wave overtopping volume increases sharply with wave amplitude, underscoring the significant risks posed by extreme waves with large amplitudes to seawall structural integrity and the potential for coastal flooding.

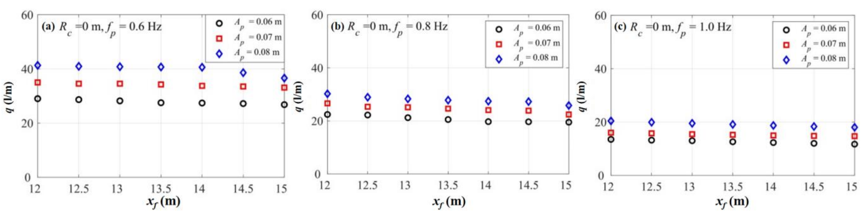

Fig. 11. Variations of wave overtopping volume per unit width (i.e., q) with focusing wave amplitude A_p and focusing location x_f.

3.3.2. Influences of wave focusing location

The occurrence of extreme waves in real nearshore environments is inherently stochastic. This section investigates the influence of the wave group focusing location (x_f) on overtopping volume to understand the potential impacts of spatial randomness. Under the experimental conditions, overtopping volumes per unit width were compared for seven focusing locations, ranging from $x_f = 12$ m to 15 m in 0.5 m intervals. As illustrated in

Fig. 11, for fixed R_c, A_p and f_p, extreme waves focusing at $x_f = 12$ m generate the highest overtopping volume. As the wave focusing location shifts closer to the shoreline (i.e., x_f from 12 m to 15 m), the overtopping volume decreases, with reductions ranging from 0.18 L/m to 4.30 L/m. This trend is attributed to the loss of wave group energy by the time the wave group reaches the seawall, thereby diminishing overtopping intensity. It is worth noting that the influence of x_f on overtopping volume is relatively minor compared to the effect of focusing wave amplitude. For example, at $f_p = 0.6$ Hz and $A_p = 0.06$ m, the overtopping volumes for $x_f = 12$ m and 15 m are 29.29 L/m and 27.07, respectively, corresponding to a reduction of 7.6%. Similarly, the reduction rates for $A_p = 0.07$ m and $A_p = 0.08$ m are 5.2% and 11.1%, respectively.

3.3.3. Influences of spectral peak frequency

To investigate the influence of spectral peak frequency on overtopping volume, the overtopping volumes associated with extreme waves at $f_p = 0.6$ Hz, 0.80 Hz, and 1.0 Hz are compared. As shown in Fig. 12, for fixed R_c, A_p and x_p, extreme waves with $f_p = 0.6$ Hz produce the highest overtopping volume, followed by f_p = 0.8 Hz, with the lowest overtopping volume observed at f_p = 1.0 Hz. This trend can be attributed to the fact that waves with lower spectral peak frequencies contain a larger proportion of low-frequency long waves, which exhibit relatively moderate nonlinear interactions during wave run-up and retain their energy until breaking at the seawall crest. In contrast, waves with higher spectral peak frequencies have a higher proportion of high-frequency components, which break prematurely on the seaward slope of the seawall, dissipating their energy and resulting in lower overtopping volumes. Quantitatively, in cases of more intensive overtopping (i.e., R_c = 0 m and A_p = 0.08 m), when f_p increases 0.6 Hz to 1.0 Hz, the average overtopping volume across the seven studied x_f cases decreases by 20.81 L/m, corresponding to a reduction of 50%. For relatively moderate overtopping cases (i.e., R_c = 0.05 m and A_p = 0.06 m), the average overtopping volume decreases by 6.27 L/m, representing a 66.7% reduction.

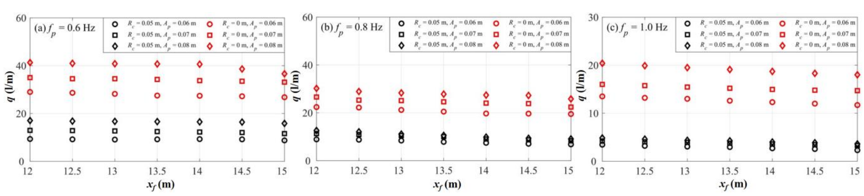

Fig. 12. Variations of wave overtopping volume per unit width (i.e., q) with spectral peak frequencies f_p and seawall crest elevation R_c.

3.3.4. *Influences of seawall crest elevation*

Extreme waves are often accompanied by local sea level rises (e.g., those caused by storm surges), which causes the seawalls to be low-crested ones. Hence, the influences of seawall crest elevation (R_c) on overtopping are studied. As depicted in Fig. 12, as the seawall crest elevation reduces from 0.05 m to 0 m, the overtopping volume increases from 9.73 L/m to 23.38 L/m, more than double. This substantial increase is evident across all cases, demonstrating that seawall crest elevation is a critical parameter influencing extreme wave overtopping volume. This underscores the wave overtopping risk under extreme wave conditions with higher water levels, i.e., smaller R_c.

3.3.5. *Summary of findings on overtopping volume*

In summary, the above analyses suggest that the seawall crest elevation exerts the most significant influence on overtopping volume under extreme wave conditions, while the impacts of focusing wave amplitude, spectral peak frequency, and focusing location are comparatively less pronounced. Of these, the wave focusing location has the least impact. Based on this, the wave overtopping volume across seven wave focusing locations are averaged for each combination of case parameters (i.e., R_c, f_p and A_p). Table 2 presents the average overtopping volumes for two R_c, three A_p and three f_p. As f_p increases from 0.60 Hz to 1.0 Hz, the average overtopping volume decreases by 6.27 L/m (a reduction of two-thirds) in the relatively mild overtopping condition (i.e., R_c = 0.05 m and A_p = 0.06 m) and by 20.81 L/m (a reduction of one-half) in the relatively violent overtopping condition (i.e., R_c = 0.0 m and A_p = 0.08 m). Additionally, Table 2 indicates that under wave conditions of low frequency and large amplitude, the influence of reducing seawall crest elevation on overtopping volume is more pronounced. For example, for the same focusing wave amplitude, the increase in overtopping volume for f_p = 0.6 Hz is approximately twice that of f_p = 1.0 Hz; at the same spectral peak frequency, the increase in overtopping volume for A_p = 0.08 m is about 1.4 times than that of A_p = 0.06 m.

Table 2. Average overtopping volume under different conditions

R_c (m)	A_p (m)	Average overtopping volume(L/m)		
		f_p = 0.6 Hz	f_p = 0.8 Hz	f_p = 1.0 Hz
0.05	0.06	9.16	7.89	2.89
	0.07	12.41	9.84	3.76
	0.08	16.56	10.66	4.21
0	0.06	27.82	20.74	12.61
	0.07	34.10	24.56	15.26
	0.08	39.94	27.95	19.13

3.4. Hydrodynamic loading on the seawall

When extreme waves overtop a seawall, the resulting breaking phenomena generate significant dynamic loads that challenge the structural integrity of the seawall. This section examines the wave overtopping induced impact pressures on the front slope, crest, and rear slope of the seawall under extreme wave conditions.

3.4.1. Time series of local pressures on the seawall

This section examines the time-varying characteristics of wave impact pressures on the seawall during overtopping, primarily based on the case with the most intense overtopping (i.e., R_c = 0 m, A_p = 0.08 m, f_p = 0.6 Hz and x_f = 13.5 m). As shown in Fig. 13, the maximum overtopping pressures at all measurement locations, except for P6, are generated by the primary wave crest. At P6, the maximum pressure is generated by the secondary trailing crest. The time series of overtopping pressure reveals that, apart from P9, multiple distinct pressure peaks are observed at P1 through P8 during the overtopping process.

On the seaward slope of the seawall, P1 records the highest overtopping pressure from the primary wave crest (hereafter referred to as "primary crest pressure"), reaching 1.41 kPa. This value is significantly higher than the pressures induced by secondary crests on either side ("secondary crest pressure"), with the primary crest pressure being approximately four times larger. At P2 that is located further upslope, the primary crest pressure decreases sharply to 0.89 kPa, while the impact pressures by the secondary crests that have moderate values do not change significantly. Such general trends are attributed to the behaviour of extreme waves as they run up along the seaward slope. During run-up, the wave train continuously breaks (resulting in energy dissipation) and a portion of the wave's kinetic energy is converted into gravitational potential energy, which lead to the impact pressures of overtopping flows decreasing progressively along the seaward slope.

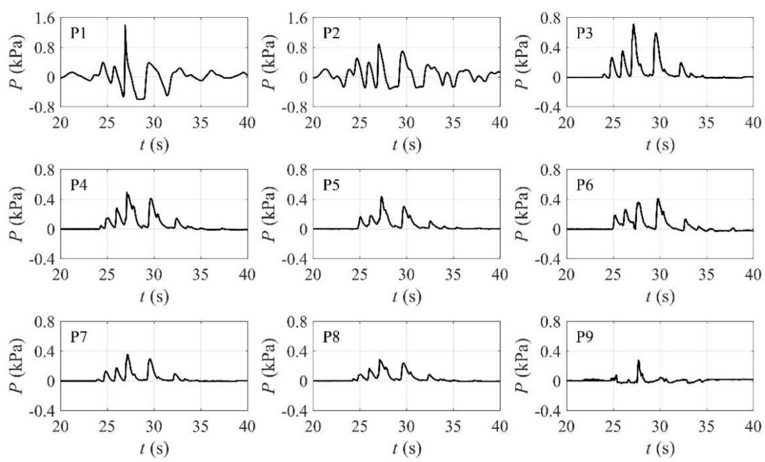

Fig. 13. Time series of impact pressures induced by overtopping flows at P1 - P9 under the condition of R_c = 0 m, A_p = 0.08 m, f_p = 0.6 Hz, and x_f = 13.5 m.

On the seawall crest, the time series of overtopping pressures at P3 to P5 shows distinct pressure peaks. These peaks are generated by the primary wave crest, as well as the secondary and tertiary crests on either side. This observation suggests that the overtopping pressure on the crest is primarily caused by the primary wave crest and the closely following secondary crests, consistent with the finding that wave overtopping in low-crested seawalls under extreme waves is predominantly caused by the primary and secondary trailing crests. Intense wave breaking on the crest leads to significant energy dissipation, resulting in a progressive decrease in overtopping pressure along the crest. Accordingly, the abovementioned pressure peaks show a declining trend as they propagate along the crest.

On the rear slope of the seawall, the maximum overtopping pressure at P6 is generated by the secondary trailing crest. This is likely because, as the primary crest reaches the rear edge of the seawall crest, it forms a jet that fully breaks before reaching P6 (see Fig. 14). Consequently, P6 is not fully impacted by the primary crest. Instead, the secondary trailing crest flows down the rear slope, directly impacting P6 and resulting in slightly higher pressure than that produced by the primary crest. At P7 and P8, both the primary and secondary trailing crests contribute to the overtopping pressure, while P9 is influenced only by the primary crest. A comparison of the overtopping pressure time series from P6 to P9 shows that the maximum pressure on the rear slope decreases progressively along the slope. This decrease is related to the energy dissipation caused by wave breaking, which reduces its impact pressure. With wave propagation, the primary crest pressure exhibits only a modest decrease, while the secondary crest pressure drops significantly (eventually reaching negligible levels). This indicates that the secondary trailing crest loses energy more rapidly than the primary crest as it propagates along the rear slope of the seawall.

Fig. 14. Overtopping pattern of the overtopping jet flow just as it contacts the rear slope at position P6 during the extreme wave overtopping process.

3.4.2. Variation of the maximum impact pressures by overtopping

(1) Influences of wave amplitude and wave focusing location

Based on the experimental cases of relatively intense wave overtopping (i.e., $R_c = 0$ m and $f_p = 0.6$ Hz), the influences of focusing wave amplitude and wave focusing location on the peak impact pressure are analysed, with the results presented in Fig. 15. Generally, for a fixed wave focusing location, the peak impact pressure on the seawall increases linearly with focusing amplitude. Conversely, for a fixed focusing amplitude, the peak pressure decreases as x_f shifts towards the shoreline. These trends align with the observed variation of wave overtopping volume as a function of wave amplitude and wave focusing location. Among the cases studied, the highest impact pressure occurs at P1, reaching 1.77 kPa, indicating that P1 is subjected to the most violent wave impacts.

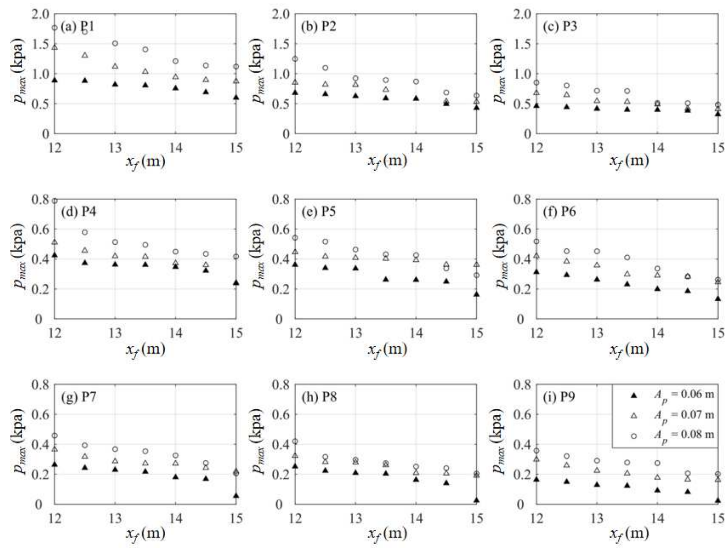

Fig. 15. Variations of peak slamming pressures at P1 to P9 with focusing amplitude A_p and focusing location x_p for the case of R_c = 0 m and f_p = 0.6 Hz.

To provide a more detailed evaluation, cases with fixed R_c, f_p and x_f are selected as illustrative examples. Using the peak impact pressure induced by an extreme wave with a focusing amplitude of A_p = 0.06 m as the baseline, the rates of increase in impact pressures at P1 – P9 as A_p increases from 0.06 m to 0.08 m are calculated and summarised in Table 3. The results reveal that on the seaward slope of the seawall, the impact pressure at P1 increases by 80.2%, which exceeds the 55.0% increase at P2, indicating that impact pressures at P1 are more sensitive to variations in wave amplitude. Notably, at P1, where the most violent impacts occur, the peak impact pressure exhibits a 99.1% increase as A_p rises from 0.06 m to 0.08 m. On the seawall crest, the increase rates at P3, P4, and P5 are comparable, measuring 61.3%, 51.0%, and 54.7%, respectively. On the rear slope of the seawall, the rate of pressure increase generally becomes larger as the measurement location moves towards the shoreline, with the growth rates exceeding 100% in some cases.

Table 3. Increase rates of peak impact pressures at P1 to P9 for the cases of R_c = 0 m and f_p = 0.6 Hz as A_p increases from 0.06 m to 0.08 m

Measurement locations	Rates of pressure peak increase when A_p increases from 0.06 m to 0.08 m (%)						
	x_f = 12	x_f = 12.5	x_f = 13	x_f = 13.5	x_f = 14	x_f = 14.5	x_f = 15
P1	99.05	92.64	83.83	74.59	60.24	64.62	86.67
P2	83.47	66.57	47.69	51.71	49.14	38.50	48.05
P3	84.79	82.06	72.51	78.33	28.58	32.79	49.77
P4	85.85	55.09	41.47	37.07	29.46	34.77	72.93
P5	50.00	51.85	37.51	64.71	63.40	35.22	80.08
P6	65.67	54.45	72.36	78.13	69.18	52.59	96.97
P7	73.86	62.42	59.92	63.27	81.32	63.03	273.75
P8	67.13	41.89	41.91	34.60	54.48	72.22	727.68
P9	118.36	115.10	126.39	126.82	200.06	152.52	783.94

(2) Influences of spectral peak frequency

Based on the cases with R_c = 0 m and A_p = 0.08 m, the influences of the spectral peak frequency on peak impact pressures are investigated. Fig. 16 shows that the peak impact pressures at P1 to P9 rise as f_p decreases, consistent with the variation trend of overtopping volume. Analyzing the peak pressures at P1 to P9 as f_p decreases from 1.0 Hz to 0.6 Hz, it is found that the changes of peak pressures with x_f are within 1.23% to 4.87%, being not significant. Accordingly, the peak impact pressures among the cases with different x_f are averaged. Based on the averaged values, the increase rates of the peak impact pressures when f_p changes from 1.0 Hz to 0.6 Hz are analyzed, as shown in Table 4. It can be seen that the peak impact pressure increases more significantly on the seaward slope of the seawall as compared to that on the seawall crest and rear slope. Notably, P1 exhibits the highest overtopping pressure and is the most sensitive to the change of f_p. The peak pressure at P3 (located near the front edge of the crest) is also evidently affected by f_p, while the peak pressures at locations closer to the shoreline (i.e., P4 to P9) are less sensitive to f_p.

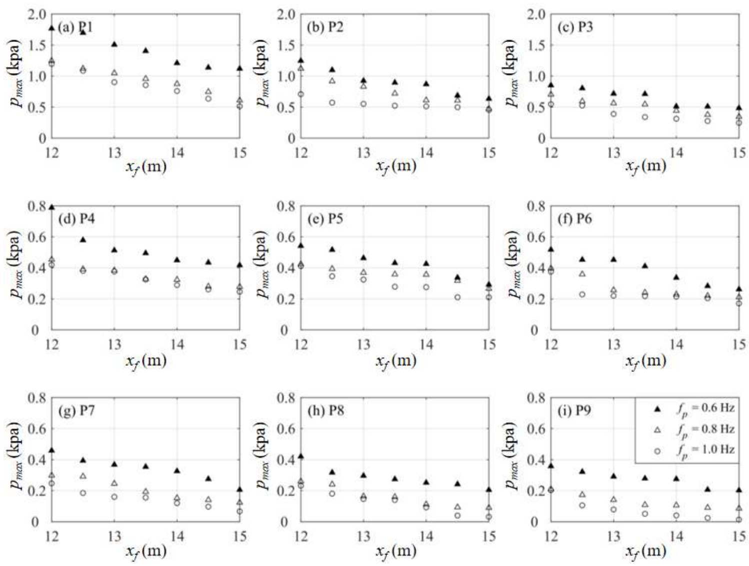

Fig. 16. Variations of peak slamming pressures at P1 to P9 with spectral peak frequency f_p and focusing location x_f for the case of R_c = 0 m and A_p = 0.08 m.

Table 4. Increase rates of peak impact pressures at P1-P9 for the cases of R_c = 0 m and A_p= 0.08 m (the values of different x_f are averaged) as f_p changes from 1.0 Hz to 0.6 Hz

Measurement locations	P1	P2	P3	P4	P5	P6	P7	P8	P9
Increase rates of impact pressure (%)	55.6	36.1	27.8	19.6	13.6	15.4	19.3	16.3	20.2

(3) Influences of seawall crest elevation

Using cases with A_p = 0.08 m and f_p = 0.6 Hz, the variation of peak impact pressures on the seawall with crest elevation R_c is examined. As shown in Fig. 17, the peak impact pressures at points P_1 to P_9 increase significantly as R_c decreases. This occurs because a lower seawall crest elevation allows extreme waves under similar conditions to carry more water during overtopping, resulting in higher kinetic energy and hence consequently a substantial rise in slamming pressures on the seawall. For quantitative analysis, the peak impact pressures at each location are averaged for cases with the same R_c and varying x_f. The results indicate that when R_c decreases from 0.05 m to 0 m, the peak pressures at P1 and P2 increase by 0.49 kPa and 0.48 kPa, respectively. On the seawall crest, the increases are relatively smaller, measuring 0.29 kPa, 0.25 kPa and 0.19 kPa at P3, P4 and P5, respectively. On the rear slope of the seawall, the rise in peak pressures due to the reduction in R_c becomes even less pronounced. These findings suggest that impact pressures at locations closer to the sea are more strongly affected by changes in crest elevation.

In summary, the peak impact pressures on a seawall induced by overtopping flows increase with greater focusing amplitude, lower spectral peak frequency, and reduced seawall crest elevation, while they decrease as the wave focusing location (x_f) shifts towards the shoreline. These trends are consistent with those observed for overtopping volume in relation to these parameters. Additionally, impact pressures at locations on the seaward slope and near the front edge of the seawall crest are generally more sensitive to wave parameters and water depth.

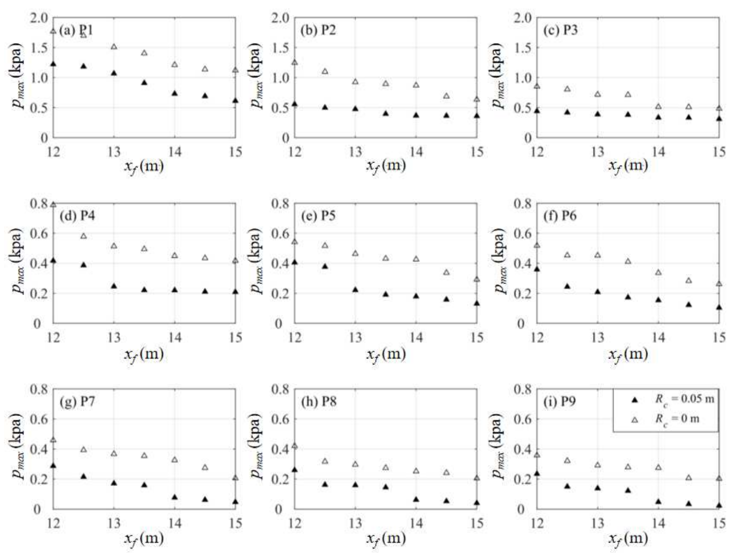

Fig. 17. Variations of peak slamming pressures at P1 to P9 with seawall crest elevation R_c and focusing location x_f for the case of A_p = 0.08 m and f_p = 0.6 Hz.

4. Conclusions and perspectives

This study has conducted well-controlled wave flume experiments to investigate the overtopping mechanisms of extreme waves on low-crested seawalls. Extreme waves were modeled using the linear focusing of a wave train. The experiments measured wave elevations at typical locations, wave profiles during overtopping, wave impact pressures on the seaward slope, crest and rear slope of the seawall, and overtopping volume per unit width. The morphological and dynamic features of the overtopping flows have been analyzed. The key findings are summarized below:

(1) Wave breaking and energy dissipation: As the spectral peak frequency and seawall crest elevation increase, the primary wave crest tends to break earlier on the seawall's front slope. This results in intensified breaking and significant energy dissipation. Additionally, when the wave focusing location of the wave train shifts closer to the shoreline, the energy reaching the seawall toe decreases, leading to reduced overtopping volumes and wave impacts.

(2) Influences of wave parameters on overtopping volume: Larger wave heights, lower spectral peak frequencies, reduced seawall crest elevations (i.e., larger water levels) and seaward shifts in wave focusing location result in more overtopping volume. Quantitatively:

i) The maximum overtopping volume in the studied cases reaches 40.50 L/m, occurring when $R_c = 0$ m, $f_p = 0.6$ Hz, $A_p = 0.08$ m and $x_p = 12.0$ m. The minimum overtopping volume is 12.12 L/m, occurring when $R_c = 0$ m, $f_p = 0.6$ Hz, $A_p = 0.06$ m and $x_p = 15.0$ m.

ii) Reducing the seawall crest elevation from 0.05 m to 0 m results in a substantial increase in overtopping volume, from 9.73 L/m to 23.38 L/m, more than doubling the overtopping discharge. Reducing the spectral peak frequency from 1.0 Hz to 0.6 Hz increases the overtopping volume from 6.27 L/m to 20.81 L/m. A shoreward shift in the wave focusing location (i.e., x_f from 12 m to 15 m) results in slight reductions in overtopping volume, ranging from 0.18 L/m to 4.30 L/m.

iii) These observations reveal a hierarchy of influences on overtopping volume, with seawall crest elevation exerting the strongest effect, followed by spectral peak frequency, focusing amplitude, and focusing location.

(3) Pressure distributions and variations: The impact pressures by overtopping flows of different wave parameters indicate that the peak impact pressure occurs at P1 with a value of 1.77 kPa, which corresponds to the case of $A_p = 0.08$ m, $R_c = 0$ m, $f_p = 0.6$ Hz and $x_f = 12.0$ m. At P1 where violent impacts happen, the peak impact pressure increases by 99.1% when the focusing amplitude A_p increases from 0.06 m to 0.08 m.

The insights gained from this study have significant implications for coastal engineering, particularly in the design and maintenance of low-crested seawalls to mitigate risks posed by extreme wave events. Key applications include:

i) Improved seawall design: the quantification of overtopping and pressure distribution enables engineers to refine seawall geometries, such as crest height and slope gradients, to balance safety and construction costs.

ii) Risk assessment and adaptation: the findings provide theoretical bases for assessing the vulnerability of coastal infrastructure under varying wave conditions, including scenarios exacerbated by climate change and sea-level rise.

iii) Wave energy management: understanding the spatiotemporal evolution of wave energy facilitates the development of energy-dissipative devices and materials to enhance coastal resilience.

While this study provides a comprehensive understanding of overtopping dynamics, several avenues for further research are identified to extend its scope, such as the influence of complex bathymetry (future studies could explore how variations in seabed topography affect wave-seawall interactions and overtopping behaviours), the impact of multi-directional waves (investigating the effects of oblique or multi-directional waves would offer a more realistic representation of overtopping dynamics), the material and structural innovations (research into advanced materials and novel structural designs, such as hybrid seawalls or energy-absorbing components, could further enhance the effectiveness of low-crested seawalls). By addressing these research directions, the understanding of overtopping mechanisms and their applications can be expanded, ultimately contributing to more resilient and sustainable coastal defence systems.

5. Acknowledgement

This research was partially supported by the National Key R&D Program of China (Grant No. 2023YFC3081300). The authors appreciate Mr Xu Wang and Mr Yi Zhan for their efforts in helping conducting the experiments and analyzing the data.

References

Adibhusana, MN, Lee, J-I, Kim, Y-T and Ryu, Y, 2023. Study of overtopping flow velocity and overtopping layer thickness on composite breakwater under regular wave. Journal of Marine Science and Engineering. 11 (4), 823.

Baldock, TE, Peiris, D and Hogg, AJ, 2012. Overtopping of solitary waves and solitary bores on a plane beach. Proceedings of the Royal Society A: Mathematical, Physical and Engineering Sciences. 468 (2147), 3494-3516.

Cao, D, Yuan, J, Chen, H, Zhao, K and Liu, PL-F, 2021. Wave overtopping flow striking a human body on the crest of an impermeable sloped seawall. Part I: Physical modeling. Coastal Engineering. 167, 103891.

Chen, H, Yuan, J, Cao, D and Liu, PL-F, 2021. Wave overtopping flow striking a human body on the crest of an impermeable sloped seawall. Part II: Numerical modelling. Coastal Engineering. 168, 103892.

Chen, X, Hofland, B, Altomare, C, Suzuki, T and Uijttewaal, W, 2015. Forces on a vertical wall on a dike crest due to overtopping flow. Coastal Engineering. 95, 9494-104.

Cuomo, G, Allsop, W, Bruce, T and Pearson, J, 2010. Breaking wave loads at vertical seawalls and breakwaters. Coastal Engineering. 57 (4), 424-439.

Dysthe, K, Krogstad, HE and Müller, P, 2008. Oceanic rogue waves. Annual Review of Fluid Mechanics. 40 (1), 287-310.

Esteban, GA, Aristondo, A, Izquierdo, U, Blanco, JM and Pérez-Morán, G, 2022. Experimental analysis and numerical simulation of wave overtopping on a fixed vertical cylinder under regular waves. Coastal Engineering. 173, 104097.

Gallach-Sánchez, D, Troch, P and Kortenhaus, A, 2021. A new average wave overtopping prediction formula with improved accuracy for smooth steep low-crested structures. Coastal Engineering. 163, 103800.

Goda, Y, 2009. Derivation of unified wave overtopping formulas for seawalls with smooth, impermeable surfaces based on selected CLASH datasets. Coastal Engineering. 56 (4), 385-399.

Goda, Y, 2010. Random seas and design of maritime structures. World scientific.

Grossmann, A and Morlet, J, 1984. Decomposition of Hardy functions into square integrable wavelets of constant shape. Siam Journal on Mathematical Analysis. 15, 723-736.

Hsiao, S-C, Hsu, T-W, Lin, T-C and Chang, Y-H, 2008. On the evolution and run-up of breaking solitary waves on a mild sloping beach. Coastal Engineering. 55 (12), 975-988.

Hsiao, S-C and Lin, T-C, 2010. Tsunami-like solitary waves impinging and overtopping an impermeable seawall: Experiment and RANS modeling. Coastal Engineering. 57 (1), 1-18.

Huang, JX, Qu, K, Li, XH and Lan, GY, 2022. Performance evaluation of seawalls in mitigating a real-world tsunami wave using a nonhydrostatic numerical wave model. Journal of Marine Science and Engineering. 10 (6), 796.

Hughes, SA and Thornton, CI, 2016. Estimation of time-varying discharge and cumulative volume in individual overtopping waves. Coastal Engineering. 117, 191-204.

Jiang, M-r, Zhong, W-j, Yu, J-x, Liu, P-l, Yin, H-j, Wang, S-d and Ma, Y-x, 2018. Experimental study on sloshing characteristics in the elastic tank based on Morlet wavelet transform. China Ocean Engineering. 32 (4), 400-412.

Koosheh, A, Etemad-Shahidi, A, Cartwright, N, Tomlinson, R and van Gent, MRA, 2024. Wave overtopping layer thickness on the crest of rubble mound seawalls. Coastal Engineering. 188, 104441.

Li, M, Zhao, X, Liu, Z, Lv, C, Lu, J, Luan, H and Zhu, Y, 2024. Numerical investigation on the hydrodynamic characteristics of coastal freak wave using a CIP-based model. Ocean Engineering. 313, 119402.

Liu, X, Sree, DKK and Law, AW-K, 2023. A numerical study on wave overwash on viscoelastic floating covers using smoothed particle hydrodynamics. Physics of Fluids. 35 (11), 117113.

Liu, Y, Li, S, Chen, S, Hu, C, Fan, Z and Jin, R, 2020. Random wave overtopping of vertical seawalls on coral reefs. Applied Ocean Research. 100, 102166.

Lobeto, H, Semedo, A, Lemos, G, Dastgheib, A, Menendez, M, Ranasinghe, R and Bidlot, JR, 2024. Global coastal wave storminess. Sci Rep. 14 (1), 3726.

Luo, M, Reeve, DE, Shao, S, Karunarathna, H, Lin, P and Cai, H, 2019. Consistent Particle Method simulation of solitary wave impinging on and overtopping a seawall. Engineering Analysis with Boundary Elements. 103, 160-171.

Mares-Nasarre, P, Argente, G, Gómez-Martín, ME and Medina, JR, 2019. Overtopping layer thickness and overtopping flow velocity on mound breakwaters. Coastal Engineering. 154, 103561.

Molines, J, Herrera, MP, Gómez-Martín, ME and Medina, JR, 2019. Distribution of individual wave overtopping volumes on mound breakwaters. Coastal Engineering. 149, 15-27.

Neelamani, S, Schüttrumpf, H, Muttray, M and Oumeraci, H, 1999. Prediction of wave pressures on smooth impermeable seawalls. Ocean engineering. 26 (8), 739-765.

Nikolkina, I and Didenkulova, I, 2012. Catalogue of rogue waves reported in media in 2006–2010. Natural Hazards. 61 (3), 989-1006.

Nørgaard, JQH, Lykke Andersen, T and Burcharth, HF, 2014. Distribution of individual wave overtopping volumes in shallow water wave conditions. Coastal Engineering. 83, 15-23.

Oumeraci, H, Klammer, P and Partenscky, HW, 1993. Classification of breaking wave loads on vertical structures. Journal of waterway, port, coastal, and ocean engineering. 119 (4), 381-397.

Owen, M and Steele, A, 1993. Effectiveness of recurved wave return walls.

Paape, A, 1960. Experimental data on the overtopping of seawalls by waves. Coastal Engineering Proceedings. (7), 36-36.

Pan, Y, Kuang, CP, Li, L and Amini, F, 2015. Full-scale laboratory study on distribution of individual wave overtopping volumes over a levee under negative freeboard. Coastal Engineering. 97, 11-20.

Qu, K, Wang, C, Wang, X, Yang, YP and Gao, RZ, 2024. Effects of strong wind on overtopping characteristics of tidal bores at coastal seawall. Ocean Engineering. 311, 118992.

Qu, K, Zhang, LB, Yao, Y and Jiang, CB, 2022. Numerical evaluation of influences of onshore wind on overtopping characteristics of coastal seawall under solitary wave. Ocean Engineering. 266, 112860.

Rif'atin, HQ, Magdalena, I, Dewata, D, Saengsupavanich, C and Sanitwong-na-Ayutthaya, S, 2024. Optimization of stepped revetment configuration on minimizing wave run-up and overtopping. Physics of Fluids. 36 (4), 046617.

Salauddin, M and Pearson, JM, 2019. Wave overtopping and toe scouring at a plain vertical seawall with shingle foreshore: A physical model study. Ocean Engineering. 171, 286-299.

van Bergeijk, VM, Warmink, JJ, van Gent, MRA and Hulscher, SJMH, 2019. An analytical model of wave overtopping flow velocities on dike crests and landward slopes. Coastal Engineering. 149, 28-38.

Van der Meer, JW, Allsop, NWH, Bruce, T, De Rouck, J, Kortenhaus, A, Pullen, T, Schüttrumpf, H, Troch, P and Zanuttigh, B, 2018. EurOtop: Manual on wave overtopping of sea defences and related structures, in: (Ed.)^(Eds.), ed., p.^pp.

Van der Meer, JW, Hardeman, B, Steendam, G-J, Schüttrumpf, H and Verheij, H, 2010. Flow depths and velocities at crest and landward slope of a dike, in theory and with the wave overtopping simulator. Coastal Engineering Proceedings. 1 (32), 10.

Van Doorslaer, K, De Rouck, J, Audenaert, S and Duquet, V, 2015. Crest modifications to reduce wave overtopping of non-breaking waves over a smooth dike slope. Coastal Engineering. 101, 69-88.

Wang, X, Luo, M, Karunarathna, H, Horrillo-Caraballo, J and Reeve, DE, 2025. Numerical investigation of freak wave slamming on a fixed deck structure. Coastal Engineering. 197, 104671.

Wen, H, Ren, B, Zhang, X and Yu, X, 2019. SPH modeling of wave transformation over a coral reef with seawall. Journal of Waterway, Port, Coastal, and Ocean Engineering. 145 (1), 04018026.

Wong, C-N and Chow, K-W, 2024. Modeling ocean swell and overtopping waves: Understanding wave shoaling with varying seafloor topographies. Journal of Marine Science and Engineering. 12 (8), 1368.

Zhao, X, Hou, Y, Lu, F, Shi, Z and Huang, Z, 2024. Numerical investigations of pedestrian overboard on a compound slope dike due to excessive overtopping waves. Physics of Fluids. 36 (10), 107148.